Chapter 2

Experimental Techniques

2.1 Introduction

Several experimental techniques have been used to characterise the perovskite samples studied in this thesis. These are X-ray and neutron powder diffraction, X-ray Absorption Near-Edge Structure (XANES), X-ray Fluorescence (XRF) spectroscopy, Thermogravimetric Analysis (TGA), impedance spectroscopy, Ultra-Violet, Visible and Near-Infrared (UV-Vis-NIR) spectroscopy and Scanning Electron Microscopy (SEM) in conjunction with Energy Dispersive X-ray (EDX) analysis. Additionally Density Functional Theory (DFT) and ISOTROPY calculations were used to augment different aspects of this study. This chapter describes the various techniques used in this work with a particular focus on the diffraction techniques and the Rietveld method. The Rietveld method is the technique used to refine structures against an experimental diffraction pattern, and thereby obtain the optimal crystallographic structure of a compound.

2.2 Diffraction Techniques

The powder diffraction techniques used in this study can be separated into three categories. These are conventional (laboratory) X-ray diffraction, synchrotron X-ray diffraction and neutron diffraction. Conventional X-ray diffraction was used during synthesis to monitor the progress of the reactions and to determine when a reaction had reached completion. This data was collected using two instruments, a Siemens D-5000 or a Shimadzu S-6000, both of which utilise Bragg-Brentano geometry. Use of these instruments was invaluable in determining the correct heating procedure to synthesise the highly pure and crystalline powder samples used in this study. Once high quality samples were obtained, synchrotron X-ray and neutron diffraction were used to determine the structures of these materials. These two techniques each have advantages and disadvantages, and are in many ways complimentary; ideally both are

used to fully structurally characterise a polycrystalline material. A comparison of these two techniques will be described in Section 2.2.4.

2.2.1 Conventional X-ray Diffraction

The majority of laboratory powder X-ray diffraction patterns were obtained using a Shimadzu Lab S-6000 Diffractometer (40.0 kV, 30.0 mA, divergence and scatter slits 1.0º and receiver slit 0.3 mm) using Cu-K_α ($\lambda_{\alpha 1}$ = 1.5406 Å, $\lambda_{\alpha 2}$ = 1.5444 Å) radiation. Finely ground samples were placed in sample holders with silicon sample cavities. The silicon plates in the cavities are cut parallel to the (510) axis. This results in "zero" background contribution from the sample holder to the diffraction pattern, allowing the use of small sample quantities[1]. Glass microscope slides were used to obtain a flat sample surface. Diffraction patterns were initially collected in steps of 0.02º (2θ angle) from 10-80º (2θ angles) for all samples using a continuous scan rate of 1º/minute (2θ angle). Where necessary, higher quality patterns were obtained by increasing the scanning time and/or decreasing the step size. The other diffractometer that was routinely used was a Siemens D-5000 (Cu-Kα radiation operating at 40.0 kV and 30.0 mA, divergence and scatter slits 1.0º and receiver slit 0.6 mm). Typically because of the poorer signal-to-noise of this instrument diffraction patterns were collected using step scans in steps of 0.02° with a collection time per step of 2-3 seconds.

2.2.2 Synchrotron X-ray Diffraction

Synchrotron X-ray diffraction patterns were collected at two beamlines. The most commonly used was the Australian National Beamline Facility (ANBF) at beamline 20B at the Photon Factory, KEK, Tsukuba, Japan. This is a multipurpose X-ray beamline that is used predominantly for X-ray powder diffraction, Extended X-ray Absorption Fine Structure (EXAFS) and X-ray Absorption Near-Edge Structure (XANES). This beamline was used for collecting synchrotron X-ray diffraction patterns of all compounds studied in this thesis at room temperature and in selected cases, above room temperature, up to a maximum temperature of 800 °C. The second beamline used for X-ray diffraction was BL-02B2 at SPring-8, Synchrotron Radiation

Research Institute, Hyogo, Japan. This beamline was used to obtain diffraction patterns of selected samples below room temperature, in the range of 90 to 300 K.

2.2.2.1 The Australian National Beamline Facility

In this thesis beamline 20B was used to collect both X-ray diffraction patterns and XANES spectra. This section describes the general optical setup of the beamline followed by a description of the X-ray diffractometer[2]. A description of the setup used for XANES measurements is described in Section 2.4.1. A schematic of the beamline optics is displayed in Figure 2.1[3]. X-rays in the energy range of 4.5 to 20 keV are available using this beamline with the bending magnet having a critical energy of 4 keV when the ring is in its most commonly used 2.5 GeV operating mode[4]. After the X-rays pass through the radiation shielding between the ring and the experiment hall they are guided through beryllium windows, various slits and a Si (111) monochromator in order to obtain a highly monochromatic (or more properly a very narrow range of wavelengths i.e. a small $\Delta E/E$), focused beam. The beam then enters the hutch where it can be used for measurements. One disadvantage of the optical design of this beamline is the necessity to detune the monochromator in order to eliminate higher harmonics of the wavelength being employed in the experiment. This is necessary to obtain a monochromatic X-ray beam and results in an intensity loss of about 50 %.

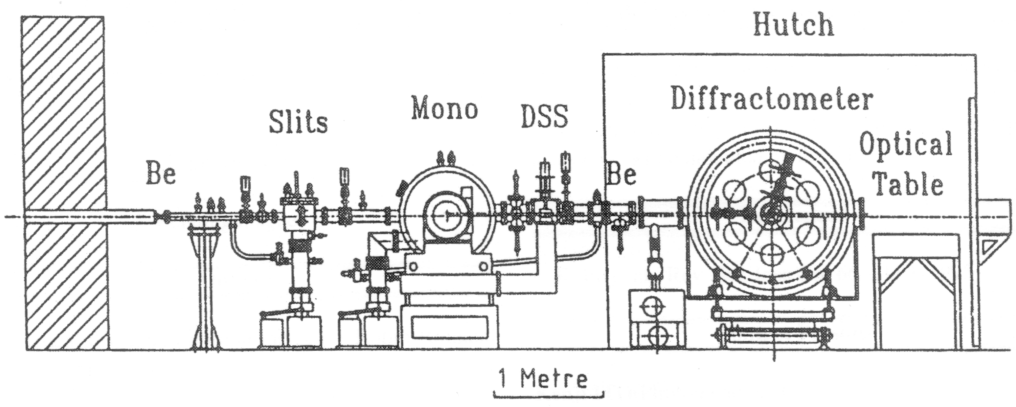

Figure 2.1: A schematic of beamline 20B, the ANBF at the Photon Factory, KEK, Tsukuba Japan[3].

Figure 2.2 presents a more detailed image of the diffractometer emphasising the experimental setup appropriate for the use of image plate detectors. This configuration was used for collection of diffraction patterns throughout this study. In the work presented in this thesis X-rays with energies of about 15 keV ($\lambda \approx 0.8$ Å) were most commonly used. The diffractometer is a Debye-Scherre camera (573 mm radius) that employs reusable image plates (spatial resolution 150 μm) manufactured by Fuji Photo Film Company Ltd. Each image plate is 200 x 400 mm thereby covering a 40° (2θ angle) range with an X-ray image being stored using a BaFBr: Eu phosphor. Image plates have a higher quantum efficiency, lower background and a much higher dynamic range compared to film[5]. The lower spatial resolution of the plates compared to film is offset by the large camera radius. Typically for room temperature measurements three image plates are used for data collection with data usually collected over the range 5-125°.

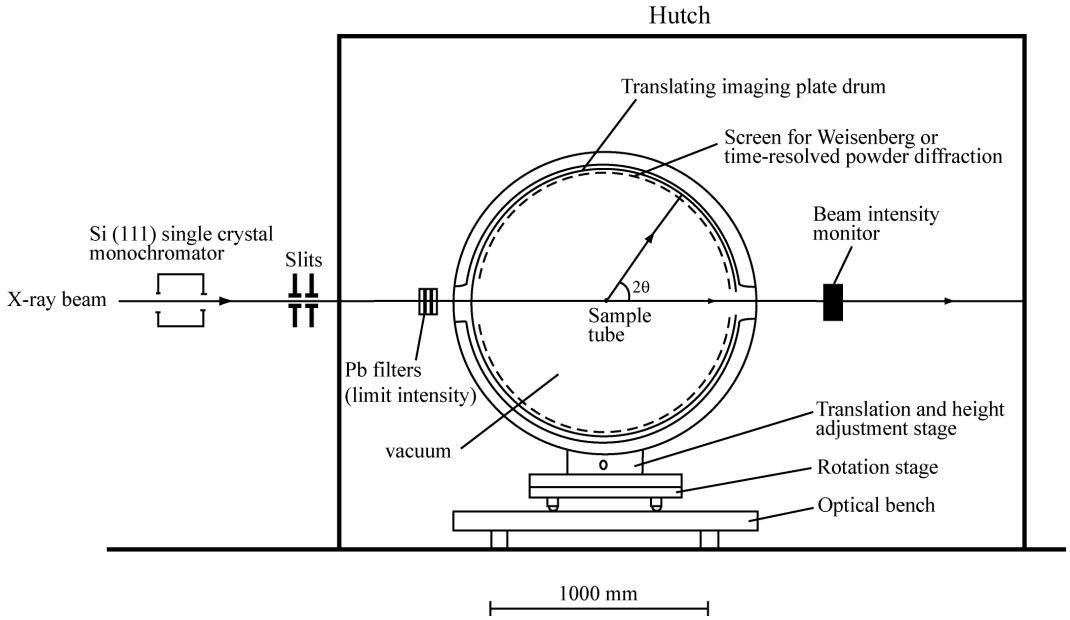

Figure 2.2: Diagram of the diffractometer in image plate mode. The figure is adapted from Barnea *et al.*[3].

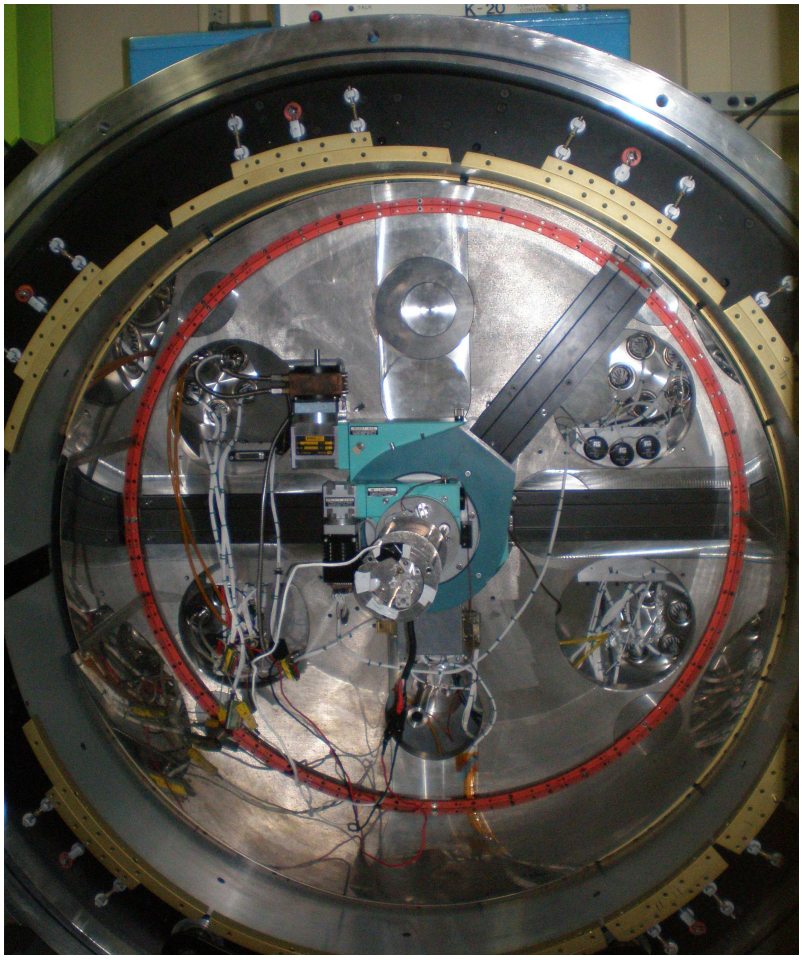

Figure 2.3: Photograph of the diffractometer at beamline 20B with the custom built furnace in place. The cassette is fully extended ready to put the image plates in.

The chamber is evacuated to a pressure of around 1.3 Pa for data collection in order to reduce X-ray scattering and absorption by air[2]. These are the major contributors to the background of the diffraction pattern. The low background in the diffraction patterns allows weak features to be detected despite the rapid rate of data collection (a typical collection time is 10 minutes per diffraction pattern). A translating image drum and associated screen (also known as the image plate cassette) allow different sections of the image plate to be exposed, allowing up to 30 diffraction patterns to be collected on one image plate. Various sample holders can be fitted, with the most commonly used in this work being a sample spinner that accommodates eight samples and a custom built furnace that is suitable for heating single specimens up to a maximum temperature of 800 °C (see Figure 2.3). It should be noted that where the furnace is employed data can only be collected using the first two image plates; that is over the approximate range of 5-85° (2θ angles). The compounds under analysis are typically

housed in a 0.3 mm diameter capillary. A small diameter capillary is preferred since in most cases this is the limiting factor determining instrumental resolution[5]. Glass capillaries are typically used for the collection of room temperature diffraction patterns while quartz capillaries are usually used for measurements at higher temperatures. A diffraction pattern of a NIST (National Institute of Standards and Technology) Si 640c standard is initially recorded so that the exact wavelength of the X-rays can be determined. Capillaries are rotated throughout the measurements to reduce the effects of preferred orientation.

After exposure the image plates are scanned using a BAS2000 image plate scanner using laser stimulated fluorescence, thereby converting the data to a digital format. The image plate scanner produces 100 μm pixels and consequently the data is collected with a step size of 0.01° (2θ angle). Data processing is carried out using the program PPDA[6], which is used to convert the data into the GSAS (General Structure Analysis System) format. This format is suitable for use in most Rietveld refinement programs. Several radioactive markers in the cassette make it possible to correlate 2θ angles with plate positions using the spots these create on the image plate.

2.2.2.2 Beamline BL-02B2

Diffraction patterns of samples studied below room temperature were collected at BL-02B2 at SPring-8 (see Figure 2.4). In addition to being able to obtain low temperature diffraction patterns at this beamline, something not readily done at the ANBF, SPring-8 is a third generation synchrotron source providing X-rays that are more highly monochromatic, intense and higher in energy than can be obtained at the Photon Factory (c.f. a critical energy of 29 keV for the BL-02B2 bending magnet to 4 keV at the ANBF[7]). This permits diffraction patterns to be collected with a shorter wavelength allowing peaks to be observed out to lower *d*-spacings while still obtaining diffraction patterns with very high resolution and intensity. While BL-02B2 is also a Debye-Scherrer camera (radius 286.5 mm) there are significant differences between this beamline and beamline 20B at the ANBF[8]. While BL-02B2 also uses a silicon monochromator it has a Ni coated silicon mirror before the monochromator that eliminates X-rays of higher harmonic frequencies of the desired wavelength. This eliminates the need to detune the optical setup as required at the ANBF and increases

the intensity of the X-rays incident on the sample[8]. The higher energies of the X-rays used at this beamline in combination with the smaller camera radius also eliminates the need to use a vacuum diffractometer because the absorption and scattering of these higher energy X-rays by air is significantly reduced.

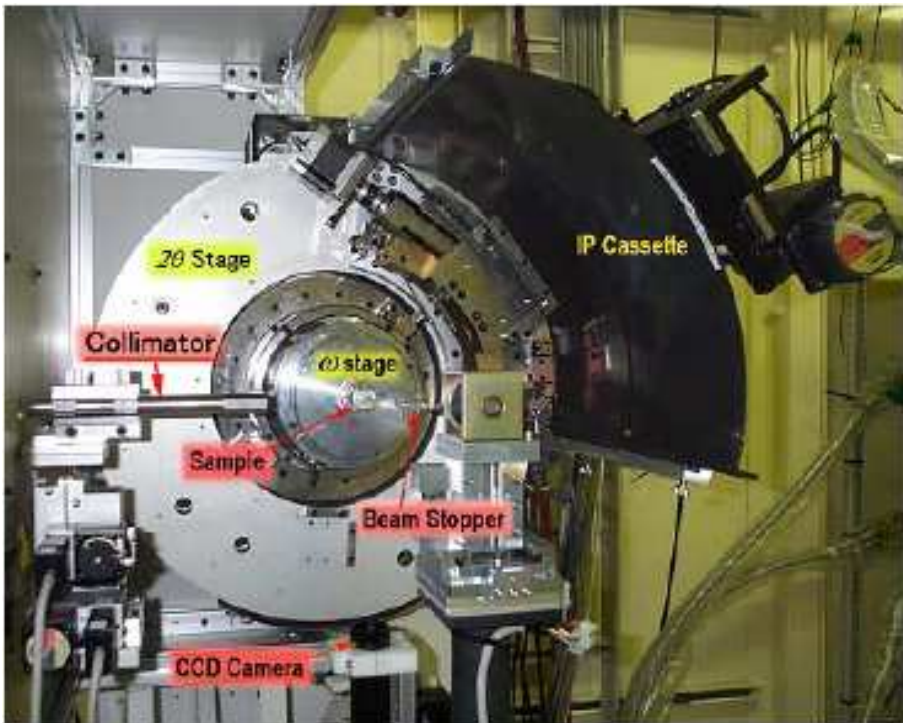

Figure 2.4: Picture of the Debye-Scherrer camera at BL-02B2 SPring-8. The image is reproduced from Takata *et al.*[9].

A single image plate (size of 200 by 400 mm with a spatial resolution of 50 μm) is employed as a detector covering an 70° (2θ angle) range in a step size of 0.01° (2θ angle)[9]. Similarly to the ANBF multiple diffraction patterns can be obtained on one image plate using a long vertical slit to expose an appropriate region of the plate. Data scanning and processing is done in a similar manner as at the ANBF. There are three sample attachments that are available; a high temperature gas flow system that can heat the sample up to 1000 K, a He cryostat capable of cooling the sample down to 15 K and a cold N_2 gas flow apparatus used for cooling the sample down to a minimum temperature of 90 K[8]. The last of these attachments was employed in the collection of diffraction patterns in this work. Data were collected using 0.6000(1) or 0.7750(1) Å X-rays over the range of 5-75° (2θ angles). Samples were mounted in 0.2 mm diameter glass capillaries and were rotated during the measurements.

2.2.3 Neutron Diffraction

There are two main methods of generating neutrons suitable for use in neutron diffraction experiments. The first of these is from the fission of a heavy nucleus, typically ^{235}U, in a nuclear research reactor. The other means of generating neutrons involves the use of a spallation source where a heavy metal target is bombarded with high energy protons generated by a particle accelerator. Upon collision enough energy is imparted to the target to produce spallation neutrons. Both of these methods produce neutrons that are too high in energy to be immediately used in a diffraction experiment. Therefore the neutrons are passed through a moderator, such as heavy water, to reduce their energy, and hence increase their wavelength, to the order of 1 Å.

Since particle accelerators produce protons in bursts neutrons made at this type of source occur in pulses. This gives rise to the fundamental difference between the types of neutron diffraction done at reactors and spallation sources. In the case of diffraction at a reactor the Maxwellian distribution of neutrons has to be passed through a monochromator to reduce the neutrons incident on a sample to a single wavelength. Typically the detector is then moved during the measurement to collect a diffraction pattern. By comparison, at spallation sources the bunched nature of the neutrons arriving at the instrument allows the use of neutrons with a wide range of different wavelengths, with the neutrons being separated by their different velocities. This allows diffraction patterns to be collected without moving the detector because each of the different neutron wavelengths will diffract off (*hkl*) planes in the structure with different *d*-spacings. Diffraction using this technique is known as time-of-flight (TOF) neutron diffraction while neutron diffraction using a single wavelength is known as continuous wave (CW) diffraction. In this thesis both types of neutron diffraction are used. The High Resolution Powder Diffractometer (HRPD) and the Medium Resolution Powder Diffractometer (MRPD), which both operated at the HIFAR (High Flux Australian Reactor) facility, and the BT1 diffractometer that operates at the NIST reactor, are good examples of reactor-based CW neutron diffractometers. Polaris at ISIS on the other hand is an example of a TOF neutron diffractometer. The use of these four diffractometers in this thesis is described in Sections 2.2.3.1 to 2.2.3.4.

2.2.3.1 High Resolution Powder Diffractometer (HRPD)

Figure 2.5: Photograph of the High Resolution Powder Diffractometer at HIFAR, Lucas Heights showing the blue coloured detector bank[10].

The HRPD was located at the HIFAR facility operated by the Australian Nuclear Science and Technology Organisation (ANSTO) at Lucas Heights in Sydney (see Figure 2.5). It operated from 1980 until the shutdown of the reactor at the end of 2006. When in operation, thermal neutrons came out of the reactor face and passed through a Soller collimator that limited the horizontal divergence of the beam to 0.20°, before passing through the monochromator[11]. The monochromator was a germanium crystal mounted with the $[\bar{1}10]$ direction vertical to bring successive (*hhl*) planes into position and operated at a take-off angle of 120° (2θ degrees). Odd index planes of the monochromator crystal were used in order to eliminate higher harmonic contamination for the commonly employed wavelengths. In this study neutrons were then directed onto the sample with a flux of ca. 5.6×10^4 or 7.2×10^4 neutrons.cm^{-2}.s^{-1} at 1.37 and 1.49 Å respectively.

Figure 2.6: Photograph of the cryofurnace attachment in operation on the High Resolution Powder Diffractometer at HIFAR[12].

The samples were usually held in thin walled vanadium cans of height 50 mm and either 12 or 16 mm diameter. Several attachments, allowing a range of different environments to be used, were shared between the HRPD and MRPD. These included a single sample spinner, a carousel capable of holding up to 30 rotating samples, a heliplex used to cool samples down to a minimum temperature of 5 K, a cryofurnace capable of a temperature range of 15-500 K (see Figure 2.6) and a P1100 furnace designed to heat over the range of 300-1400 K under a variety of atmospheres[10]. Neutrons scattered from the sample were detected using a bank of 24 ^{3}He detectors spaced 5° (2θ angle) apart, each with their own Soller collimator. Patterns were collected over a range of 5 to 150° (2θ degrees) using a step size of 0.05° (2θ degrees). In this study collection times per diffraction pattern were typically around 1-2 days.

2.2.3.2 Medium Resolution Powder Diffractometer (MRPD)

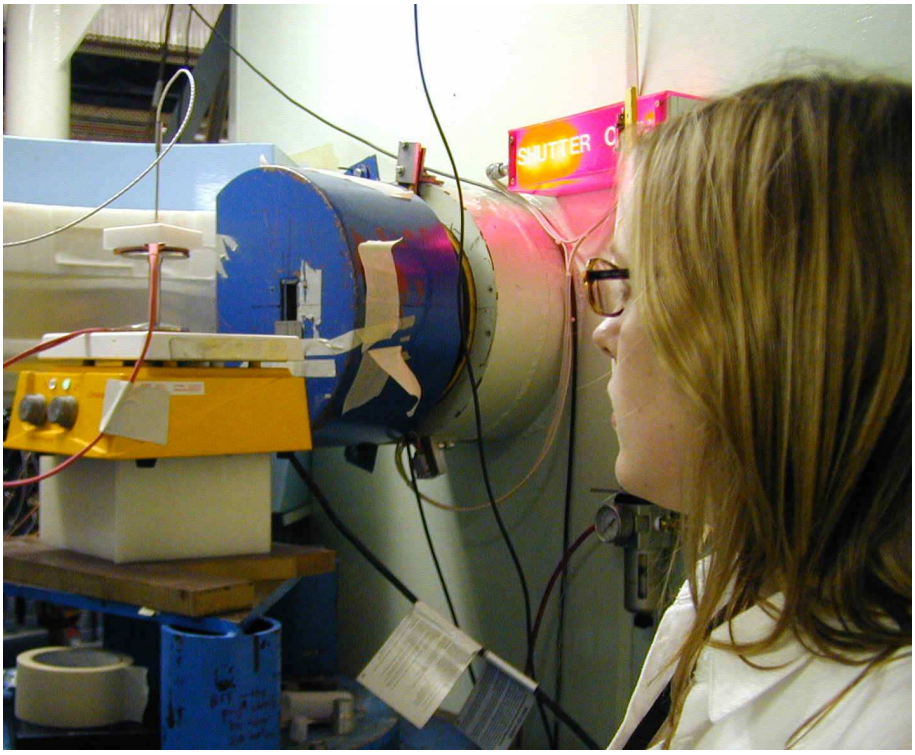

Figure 2.7: Picture of the Medium Resolution Powder Diffractometer at HIFAR[13].

The MRPD was located opposite the HRPD at the HIFAR facility (see Figure 2.7). The resolution of the MRPD was about a factor of two lower than that of the HRPD when used in high resolution mode, as is the case in this study[14]. Typically, however, it had a neutron beam with 5 times the intensity of the HRPD and was capable of collecting a typical diffraction pattern in 4 to 6 hrs[14]. The MRPD was therefore used in this work to collect variable temperature diffraction patterns in selected cases after ambient temperature characterisation was carried out using the HRPD. The monochromator consisted of 8 germanium crystals in a vertically focussing arrangement operating at a take-off angle of 100°[13]. In this study a wavelength of approximately 1.66 Å was used with a flux of ca. 1.4×10^5 neutrons.cm^{-2}.s^{-1} incident on the sample. Samples were usually held in similar cans to those used for the HRPD except where high temperature diffraction patterns were collected, where steel cans were required. A bank of 32 ^{3}He detectors, each with their own Soller collimator, allowed relatively rapid data collection over a range of 8 to 138° (2θ degrees) using a step size of 0.1° (2θ degrees)[13].

2.2.3.3 BT-1

Figure 2.8: Picture of the BT-1 High Resolution Neutron Powder Diffractometer[15].

BT-1 is a high resolution neutron powder diffractometer located at the NIST Centre for Neutron Research reactor Gaithersberg, Maryland in the United States of America (see Figure 2.8)[15, 16]. It has a flexible experimental design with a choice of three monochromators, Ge(311), Cu(311) and Ge(733), which can be used with either a 7 or 15 arcminute Soller collimator[15, 16]. This allows the user to optimise the choice between resolution and the flux of the neutrons on the sample. In the work presented in this thesis the Cu(311) monochromator was utilised, with a take-off angle of 90° (2θ degrees), in combination with the 15 arcminute collimator. This is the middle resolution setting of the instrument and provides 1.5403(1) Å neutrons with a flux of approximately 4×10^5 neutrons $s^{-1}cm^{-2}$ on the sample[15]. During the experiment samples were held at ambient temperatures in vanadium cans. Neutrons were detected using a bank of 32 He^3 detectors, each equipped with their own 7 arcminute Soller collimator, with a separation of 5° (2θ angle) between detectors[15]. Patterns were

measured over the range 3 to 167° (2θ degrees) with a step size of 0.05° (2θ degrees) requiring a collection time of approximately 5 hrs per sample.

2.2.3.4 Polaris

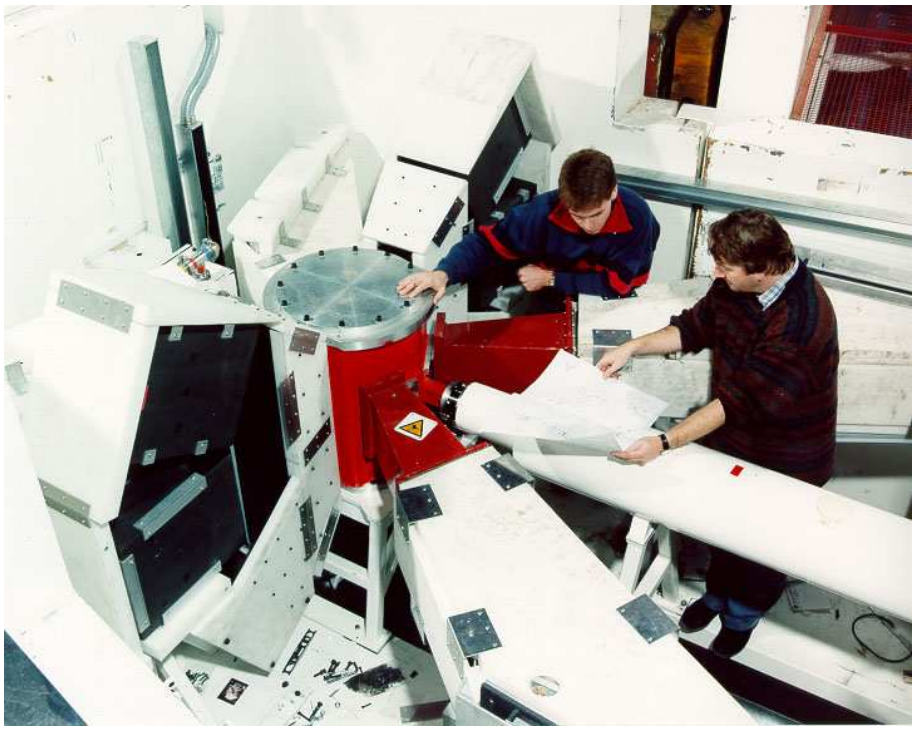

Figure 2.9: Photograph of the Polaris diffractometer at ISIS indicating the large solid angle covered by detectors[17].

Polaris is the medium resolution time-of-flight neutron powder diffractometer at the ISIS spallation neutron source, Rutherford Appleton Laboratory (RAL), Didcot, Oxfordshire in the United Kingdom (see Figure 2.9)[18, 19]. The neutrons used by the Polaris diffractometer are generated from a tantalum target and then moderated by a pool of ambient temperature water followed by gadolinium poisoning[18]. The neutrons are then guided down a 12 m primary flight path past the nimonic and B_4C chopper, which rotates at a rate of 50 Hz. The chopper eliminates neutrons that are too high or too low in energy to be of use for the measurement before they reach the sample[20]. The sample is held in a vanadium can (50 to 75 mm by 5 to 11 mm depending on sample size) in a tank that is evacuated to a pressure of ~0.1 mbar in order to reduce the attenuation of the incident and scattered neutrons[20]. This sample

tank is capable of holding a large range of standard RAL sample environments allowing measurements over a wide range of temperatures and pressures.

There are four banks of detectors, two low angle banks (one with ^{3}He detectors and another with ZnS detectors), a bank of backscattered ^{3}He detectors and a 90° bank of ZnS detectors. The wide range of solid angles covered with detectors combined with the high flux incident on the sample allows diffraction patterns to be collected very quickly or on very small sized samples[18]. Additionally because the detectors are resolution focused they have approximately constant resolution throughout their *d*-space range. These detectors also collect data to much smaller *d*-values (~0.2 Å) than a continuous wave neutron diffractometer is typically capable of. This makes Polaris ideal for studying oxygen vacancies in materials, and was therefore the main use it was employed for in this work. After a pattern is measured it is normalised using the program GENIE to account for intensity variations in the incident neutrons and background signal from the instrument and sample can before translation into the GSAS format[20]. In the analysis presented in this thesis only the backscattered bank of detectors was used, due to its higher resolution ($\Delta d/d \sim 5 \times 10^{-3}$)[20].

2.2.4 X-rays versus Neutrons

While laboratory X-ray diffraction is adequate for assessing sample purity, synchrotron X-ray diffraction and/or neutron diffraction are superior techniques for the determination of structures of complex metal oxides such as perovskites. In many ways synchrotron X-ray and neutron diffraction are complimentary because they provide different information about the structure of materials. These are costly techniques and competition for use of these instruments is very high, so it is necessary to fully understand the strengths and weakness of both techniques in order to understand when each of these should be employed.

The first aspect of each technique that should be examined is the resolution. This is illustrated in Figure 2.10. It can be seen from this that synchrotron X-ray diffraction typically has much higher resolution than conventional X-ray diffraction, which in turn has higher resolution than a typical neutron diffractometer. The higher resolution available from synchrotron X-ray diffractometers is a result of the highly

monochromatic nature and, crucially, lower divergence of the X-rays available from a synchrotron[21]. The higher intensity of X-rays available from synchrotron sources is important in regards to this as it allows the X-ray beam to be highly focused and monochromated while still maintaining sufficient flux on sample to allow for rapid data collection. The higher resolution of synchrotron X-ray diffractometers results in sharper peaks in the diffraction pattern making it possible to resolve very small distortions from a metrically cubic cell that could not otherwise be observed in conventional X-ray or neutron diffraction patterns.

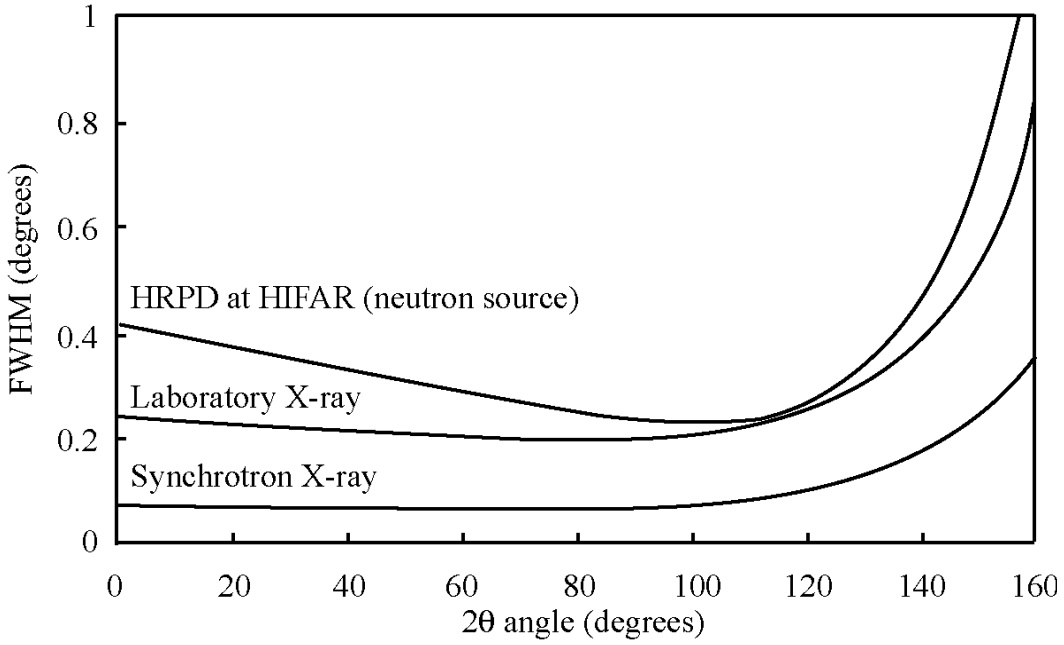

Figure 2.10: Comparison of the resolution (measured as the full-width of peaks at half maximum intensity) available from different diffraction sources[22].

There are also considerable differences between the variation of the resolution of the various techniques with increasing values of 2θ, resulting from the different diffractometer geometries. Since X-rays interact with electrons there is a rapid fall off in scattering power at high angles in X-ray diffraction[23]. Clearly it is desirable for the highest resolution to be obtained at lowest angles, where scattering is strongest, to maximise the quality of the data. It is important, however, to still have as high resolution as possible at higher angles as this enables more precise structural parameters to be obtained. With synchrotron X-ray diffraction this can, in part, be achieved by selecting a shorter wavelength and therefore obtaining lower *d*-values at

the same 2θ angle compared to those obtainable from a typical conventional diffractometer. Using a shorter wavelength to collect a synchrotron X-ray diffraction experiment, however, also leads to less angular separation between peaks in the pattern so care must be taken to ensure that the splitting of peaks, particularly at lower angles can still be observed. On the other hand in neutron diffraction the neutrons diffract off the nucleus leading to their scattering efficiency remaining essentially unchanged up to high 2θ angles[23]. In order to maximise the quality of data obtained at higher 2θ values and thereby obtain more accurate atomic positions and displacement parameters a diffractometer geometry with a high monochromator "take-off" angle is typically chosen. The "take-off" angle is the angle at which the neutrons leave the monochromator, with a high angle maximising the resolution at higher 2θ angles and leading to the angular variation indicated in Figure 2.10.

It should be noted at this point that the above discussion has only considered continuous wave diffractometers and has neglected time-of-flight neutron diffraction. In general the errors in the time of flight of the neutrons used in this technique still result in poorer resolution than available from a synchrotron X-ray diffraction pattern. While this is the case for Polaris, the High Resolution Powder Diffractometer at ISIS has comparable, and in many cases, superior resolution compared to synchrotron X-ray diffractometers due to its significantly longer flight path (~100 m)[24]. At present, however, this instrument remains one-of-a-kind and, while other comparable diffractometers are being developed elsewhere, obtaining time on this instrument is currently very difficult.

The second major advantage of synchrotron X-ray diffraction compared to diffraction using conventional X-ray sources and neutrons is the much higher flux obtained on sample. This results in diffraction patterns with significantly improved signal-to-noise levels making it possible to examine weak features that can not be seen in a conventional X-ray diffraction pattern. This higher signal-to-noise level is further augmented by the higher resolution available from synchrotron diffractometers. This leads to the total intensity of peaks being concentrated over a narrower angular range than is the case for lower resolution diffraction patterns, increasing the height of the peak and hence leading to a higher signal-to-noise level. The combination of this with

the higher resolution and ability to tune to different wavelengths, as required, makes synchrotron X-ray diffraction a superior technique for determining the structures of materials compared to conventional X-ray diffraction. The interaction of X-rays with matter is also much stronger than that of neutrons. This further improves the intensity of the beam diffracted from the sample in synchrotron X-ray diffraction compared to neutron diffraction[23]. This means that X-ray diffraction requires both a smaller sample size (50-100 mg compared to 5-15 g for neutron diffraction) and shorter collection time (~10-15 minutes per pattern for a synchrotron X-ray diffractometer using an area detector such as an image plate compared to 2 hrs to 2 days for a neutron diffractometer).

The faster collection time and smaller sample size required makes synchrotron X-ray diffraction the ideal technique to use to structurally characterise a larger number of samples and for variable temperature measurements on samples where fine temperature steps are desired. This is the underlying reason why in this study all samples have been initially characterised by synchrotron X-ray diffraction prior to selected samples being characterised by neutron diffraction. It is also why almost all the variable temperature diffraction measurements have been carried out using synchrotron X-ray diffraction instead of neutron diffraction particularly in cases where the main objective is to obtain precise lattice parameters.

At this point it may seem that synchrotron X-ray diffraction is a better structural characterisation tool than neutron diffraction due to the higher resolution, lower background and shorter collection times available using this technique. As already mentioned, however, the way that X-rays and neutrons interact with matter is fundamentally different and this gives rise to different trends in the sensitivity of each technique with different elements. Since, in X-ray diffraction, the interaction between the elements in the sample and the X-rays is proportional to the number of electrons an element has, heavier atoms scatter X-rays far more strongly than lighter atoms (see Figure 2.11). Conversely, in neutron diffraction the interaction between neutrons and the atomic nuclei has no clear relationship with atomic number since it depends on short range nuclear forces and resonance scattering (see Figure 2.11)[23]. This can lead to significant variation in nuclear scattering between elements next to each other in the periodic table or even isotopes of the same element. This can make neutron

diffraction useful for examining structures containing two or more elements with similar atomic numbers.

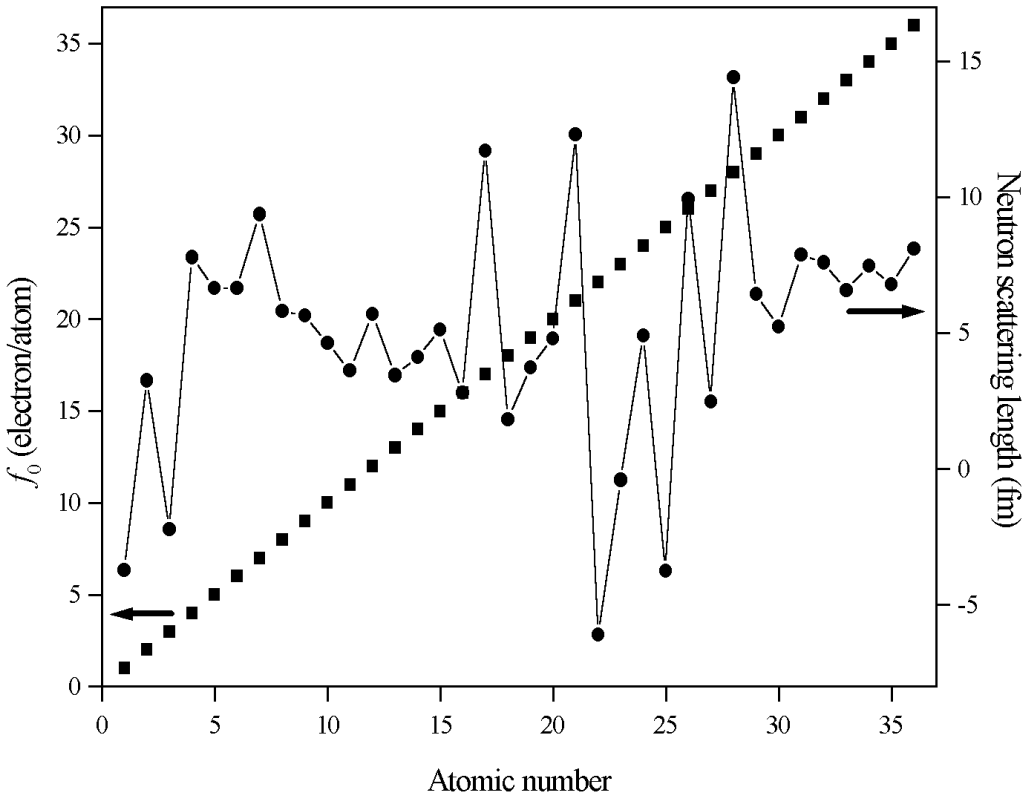

Figure 2.11: Comparison between the change in scattering strengths of X-rays (squares) and neutrons (circles), as measured by the X-ray form factor and neutron scattering length respectively, with changing atomic number. This figure has been generated from data contained in the *CRC Handbook of Chemistry and Physics*[25].

Since the neutron scattering strength of an element does not increase strongly with increasing atomic number, as is the case for X-rays, neutron diffraction is relatively more sensitive to lighter elements in the presence of heavier elements. This was particularly useful in this study where the structures of heavy metal oxides are examined. The presence of cations such as the lanthanides, barium and tantalum makes X-ray diffraction "insensitive" to the oxygen anions in the structure. There are two reasons why neutron diffraction was of great benefit for studying the perovskite structures examined in this thesis. The first of these is that the tilted perovskite structures have additional reflections, compared to the cubic structure, that have an intensity that depends primarily on the oxygen anion positions. Secondly, and most

importantly, neutron diffraction provides more accurate information about the oxygen anion positions and occupancies in the structure. This leads to a more accurate model of the bonding environments and, crucially, in the later half of this study the amount and crystallographic positions of any oxygen vacancies in the structure.

2.3 Structural Analysis

Solving the structure of a completely unknown compound directly requires either single crystal X-ray and/or neutron diffraction or, where only a powder sample of the material is available, very high quality synchrotron and/or neutron diffraction patterns in combination with *ab initio* solution methods, which are extremely time consuming, complicated and often difficult to use correctly. Either of these approaches essentially consists of four stages; determining the appropriate Bravais lattice, followed by selecting the correct space group, calculating approximate positions for the different types of atoms present and finally refining all the instrumental and sample parameters to determine an accurate structural model for the selected compound. Where, however, a material belongs to a large family of compounds for which the possible structures are well known, it is possible to establish which of these possibilities is appropriate for the diffraction pattern of a new compound and then fit this model to the pattern, thereby obtaining accurate and precise structural parameters.

The many different structures adopted by perovskites, and in particular perovskites that are only distorted from the ideal cubic perovskite by octahedral tilting and cation ordering, are well known. This knowledge comes from both experimentally determined structures and the group theoretical analysis of Howard *et al*.[26, 27] that was outlined in Chapter 1. In this work the first stage of structural analysis was to determine which of the well known variants of the perovskite structure matches the diffraction pattern collected. This was done by visually inspecting the diffraction pattern of a sample to determine both the nature of any peak splitting and any additional weak peaks that may be present. Such an inspection greatly reduces the number of possible structures that need to be considered; in ideal cases only one space group is possible.

Once the correct variant has been selected the second stage of the structural analysis was to refine a model of the selected variant against the diffraction pattern using Rietveld refinement and thereby obtain an accurate structural model of the sample[28].

At this point both the quality of the fit to the diffraction data and the chemical reasonableness of the refined model are inspected to determine if the refinement is successful and, in the case where from visual inspection it was not possible to narrow down the list of perovskite structures to one, which of the possible symmetries the structure adopts. This approach allows the structure of a compound to be determined from a polycrystalline sample and is simpler and far less computationally expensive than the use of *ab initio* techniques. Both steps of this structural analysis will now be described.

2.3.1 Visual Inspection

Visual inspection of a diffraction pattern of a perovskite can reveal additional peaks in the pattern compared to those expected from the primitive cubic structure. These can take the form of either peak splitting or additional peaks that are at significantly different positions to those expected for the primitive cubic perovskite structure.

Peak splitting indicates a deviation from the metrically cubic structure and identifying the peaks that are split can provide an insight into which of the seven possible crystal systems the structure belongs to. Different crystal systems have different diagnostic peak splitting. Consider, for example the (222) and (004) reflections of the primitive cubic structure. If the (222) peak is split into two peaks while the (004) peak is still a single peak the structure is rhombohedral. On the other hand if the (222) peak is a single peak while the (004) peak is split a tetragonal structure is indicated. The ratio of the intensities of these split peaks is also a useful indicator of which structure is adopted. This study examines the structures of both ternary and double perovskites. Following the group theoretical analysis of Howard *et al.*[26, 27], the compounds of interest could adopt any one of a total of 27 different structures. By visually determining the correct crystal system for a compound the number of likely structures can be reduced to a handful. This minimises the number of Rietveld refinements that need to be carried out to determine the correct structure. Perovskites are, however, often pseudo-cubic and it is consequently necessary to use

high resolution synchrotron X-ray diffraction patterns to establish this peak splitting. Even using synchrotron X-ray diffraction, some distorted structures still appear, metrically, to belong to a higher symmetry unit cell. Therefore, while an examination of peak splitting is very useful, it is not necessarily conclusive.

Additional peaks in the diffraction pattern, compared to those expected in the primitive structure, can also be used to assist in determining the correct symmetry. Whether these additional peaks are due to a distortion in the structure or are caused by the presence of impurities in the sample can usually be determined relatively easily because those peaks caused by a structural distortion can be indexed with one or more indices being a reciprocal integer on the primitive unit cell. For tilted perovskites additional reflections that correspond to structural distortions are *R*-, *M*- or *X*-point super-lattice reflections and relate to the type of tilting in the structure[27]. For both single and double perovskites *R*-point reflections indicate the presence of out-of-phase tilting, *M*-point reflections indicate in-phase tilting and *X*-point reflections indicate a combination of both. These reflections are named after the boundary points of the Brillouin zone where soft mode vibrations (phonons) freeze in order to create the octahedral tilting observed in the structure[27, 29]. *M*- and *R*-points correspond to the centre of an edge and a corner point in the primitive cubic perovskite respectively and freezing of the vibrations at both of these points causes the additional freezing of a vibration at the *X*-points (these are at the centre of a face)[30, 31].

Since the symmetry each tilt system belongs to has been established, by the works of both Glazer[32, 33] and Howard *et al.*[26, 27], using these additional reflections in combination with peak splitting can provide more assurance that the correct space group can be obtained by visual inspection of the diffraction pattern. In this study, however, there are two complicating factors in using these weak peaks as part of the tilt system analysis. The first of these is that the presence of rock-salt cation ordering in double perovskites also corresponds to the *R*-point of the Brillioun zone and therefore creates *R*-point reflections at the same positions in the diffraction pattern as does out-of-phase octahedral tilting[26]. Hence in the compounds in this study *R*-point reflections can indicate out-of-phase tilting and/or that the structure is that of an ordered double perovskite. Secondly, because of the heavy metals cations in the compounds studied in this project, the intensity of these super-lattice reflections in

X-ray diffraction patterns are very weak when they are caused by octahedral tilting. This is because the majority of the intensity of the super-lattice reflections in these cases is caused by the displacement of the much lighter oxygen atoms with only a smaller secondary contribution from the displacement of the A-site cations, where allowed by the symmetry of the structure. Therefore in many cases either synchrotron X-ray diffraction patterns with very low backgrounds or neutron diffraction is necessary to correctly identify these features.

2.3.2 Rietveld Method

The Rietveld method (also known as Rietveld refinement) uses a least squares fit approach to minimise the difference between the model employed and the entire diffraction pattern. This is a different methodology to earlier techniques that assigned peaks to individual reflections and calculated the structure based on those assignments. The Rietveld method is a superior approach since it does not rely on the splitting of overlapped peaks, which are very common in powder diffraction, to correctly assign individual intensities. Rather it refines a model featuring a number of parameters against the whole pattern to obtain the optimum least squared fit. Equation 2.1 is the basis of the Rietveld method, determining the calculated intensity at each point of the pattern. The variables are defined as follows; y_{ic} is the net intensity at point i, y_{ib} is the background intensity, G_{ik} is the normalised peak profile function, I_k is the intensity of the k^{th} Bragg reflection contributing intensity at point i and p is the number of phases present .

$$y_{ic} = y_{ib} + \sum_{p} \sum_{k=k_1^p}^{k_2^p} G_{ik}^{p} I_k \qquad \textbf{2.1}$$

In a Rietveld refinement there are two categories of parameters to refine; these are the instrumental parameters that are determined by the experimental apparatus employed and the sample parameters, which depend on the structure of the compound. Instrumental parameters include the zero offset, the background parameters, the peak shape parameters and where necessary absorption, extinction and preferred orientation coefficients. The sample parameters on the other hand include the lattice parameters,

the phase scale (this relates to the amount of a phase present) and the atomic position, displacement and occupancy parameters. It is these crystallographic parameters that provide the most meaningful information regarding the sample being examined. It is important to note that in general it is unwise to, at least initially, refine all the possible parameters at once. Rather it is better to refine a small number of parameters first and then increase the number of parameters as the refinement progresses. In general instrumental parameters are optimised first followed by the sample-related parameters, although the phase scale and lattice parameters are often refined early in the procedure. Throughout this thesis refinements were commonly carried out using the program Reitica[34] or, in the case of neutron time-of-flight data, GSAS[35].

The background parameters are one of the first fitted. Two main methods were used to model the background. The first of these is the selection of up to 50 points that are interpolated to determine the background. This type of background was most commonly used to model the first histogram of synchrotron X-ray diffraction patterns. This is because of the broad peaks in the pattern caused by the amorphous glass or silica capillaries used as a sample holder. Parametric backgrounds typically do not provide an adequate fit to these broad peaks. The second type of background model used is a 6^{th} order polynomial (see Equation 2.2) where B_m is one of six refinable functions. This type of background is used in the majority of neutron diffraction patterns and in the second and third histogram of synchrotron X-ray diffraction patterns. In the case of TOF neutron diffraction a Chebyschev polynomial function is used instead of the standard polynomial in order to obtain a better fit.

$$y_{ib} = \sum_{m=-1}^{n} B_m (2\theta)^m \qquad \textbf{2.2}$$

Another critical set of instrumental parameters are the peak shape parameters. Throughout the present work pseudo-Voigt peak shape was employed. This is because of the superior fit obtained using this model and its ability to fit both X-ray and neutron diffraction patterns well by varying the Lorentzian and Gaussian components of the peak shape. In the case of continuous wave diffraction experiments the pseudo-Voigt function is as defined in Equation 2.3 where $C_0 = 4$, $C_1 = 4ln2$, H_k is the full

width at half maximum (FWHM) of the k^{th} Bragg reflection, $X_{ik} = (2\theta_i - 2\theta_k)/H_k$ and γ is a refinable "mixing" parameter with $\gamma = 0$ and 1 being the Gaussian and Lorentzian limiting cases respectively[34].

$$G_{ik} = \gamma \frac{C_0^{1/2}}{H_k \pi} \left[1 + C_0 X_{ik}^2\right]^{-1} + (1-\gamma) \frac{C_1^{1/2}}{H_k \pi^{1/2}} exp\left[-C_1 X_{ik}^2\right] \quad \textbf{2.3}$$

The FWHM function is defined by Equation 2.4[34]. It should be noted that during a refinement it is the *U, V, W* and γ parameters that are refined when modelling a continuous wavelength diffraction pattern. Where necessary an asymmetry correction can be applied with the Howard asymmetry correction being used in this study because it is a more physically appropriate correction for peak asymmetry in continuous wavelength measurements[34].

$$H_k^2 = U \tan^2\theta + V \tan\theta + W \quad \textbf{2.4}$$

TOF neutron diffraction patterns have a significantly different peak shape from continuous wave measurements and therefore require a different type of peak shape function, as is defined in Equation 2.5. α and β are exponential decay terms defined to vary with *d*-spacing, *d*, as $\alpha = \alpha_0 + \alpha_1/d$ and $\beta = \beta_0 + \beta_1/d^4$. The functions *Erfc* and E_1 are the complex error function and complex exponential integral function, respectively and η is dependant on the ratios of the Lorentzian and Gaussian FWHM functions. The other terms are defined as $u = 0.5\alpha\left(\alpha\sigma^2 + 2X_{ik}\right)$, $v = 0.5\beta\left(\beta\sigma^2 + 2X_{ik}\right)$, $y = \left(\alpha\sigma^2 + X_{ik}\right)/\left(\sqrt{2}\sigma\right)$, $z = \left(\beta\sigma^2 - X_{ik}\right)/\left(\sqrt{2}\sigma\right)$, $p = -\alpha X_{ik} + i\alpha\gamma/2$, $q = -\beta X_{ik} + i\beta\gamma/2$ and $X_{ik} = (\mathrm{TOF}_i - \mathrm{TOF}_k)/\mathrm{H}_k$ where H_k is the overall FWHM function. The overall FWHM function has a more complex dependency on separate Gaussian and Lorentzian peak-shape functions (that are proportional to σ and γ respectively) than is the case for continuous wave diffraction. These three FWHM functions are described in Larson and Von Dreele [35].

$$G_{ik} = \frac{\alpha\beta}{2(\alpha+\beta)}\left[(1-\eta)\left(e^{u}Erfc(y)+e^{v}Erfc(z)\right)-\frac{2\eta}{\pi}Im\left(e^{p}E_1(p)+e^{q}E_1(q)\right)\right] \quad \textbf{2.5}$$

Once the instrumental parameters have been refined the sample parameters can be modelled. Of these, the lattice parameters, in combination with the diffractometer zero offset, determine where the model peaks are in the diffraction pattern. Atomic positions, displacement parameters and occupancies influence various aspect of peak intensity. Atomic positions and occupancies affect the intensity of peaks while the displacement parameters influence the rate that peak intensity decreases and broadens at with decreasing *d*-spacing. There is a strong correlation between these three types of parameters requiring data to be collected over a large range of *d*-space to determine accurate and precise values for these parameters, particularly where information regarding occupancies is desired.

After instrumental and sample parameters have been refined it is then necessary to judge the quality of the refinement. This is particularly important in the case where a comparison between a number of possible perovskite structures is required. The quality of a refinement can be judged in two ways. The first is an examination of various statistical measures of the quality of the fit. These measures include the profile factor R_p, the weighted profile factor R_{wp} and the goodness of fit term χ^2 (defined in Equations 2.6 to 2.8).

$$R_p = \frac{\Sigma\left|y_{iobs} - y_{icalc}\right|}{\Sigma y_{iobs}} \quad \textbf{2.6}$$

$$R_{wp} = \left[\frac{\Sigma w_i\left(y_{iobs} - y_{icalc}\right)^2}{\Sigma w_i y_{iobs}^2}\right]^{\frac{1}{2}} \quad \textbf{2.7}$$

$$\chi^2 = \frac{\Sigma w_i\left(y_{iobs} - y_{icalc}\right)^2}{N - P} \quad \textbf{2.8}$$

Where: y_{iobs} is the set of observed diffraction intensities collected at each step across the pattern,

y_{calc} is the set of corresponding calculated values,

w_i is the weight assigned to the individual step intensity given by $w_i = \frac{1}{\sigma_i^2}$ where σ_i^2 is the variance at the i^{th} step

N is the number of observations, i.e. the total number of y_{iobs}'s when the background is refined and

P is the number of refined parameters.

While ideally the lowest possible values of these factors should be obtained, in practise addition of more parameters to the refinement, such as additional background parameters and adding extinction and/or absorption corrections, to obtain a minor improvement in the fit should be avoided in order to prevent over-parameterisation. Additionally it must be remembered that different types of diffraction patterns tend to have widely varying values for these measures of fit. A good example of this is χ^2, which has a value greatly influenced by the signal-to-noise of the diffraction pattern. As a result of this while an acceptable χ^2 for a synchrotron X-ray diffraction pattern recorded at the ANBF may be in the order of a few hundred, because of the very low background obtainable using this instrument, such a value for a neutron diffraction pattern would be completely unacceptable, in this case a value in the order of one is desired. Therefore statistical measures should only be used to compare different fits to the same diffraction pattern or the effect of adding additional parameters to a refinement.

The second measure of the success of a refinement is a visual inspection of the fit to the pattern. The fit can be evaluated by examining the difference plot to ensure there are no systematic discrepancies between the diffraction pattern and the model fitted to it. The fitted diffraction pattern can also be inspected to ensure that any subtle splitting is replicated by the fitted model. Additionally the instrumental and structural parameters should also be checked in order to make sure they, and hence the model, are physically and chemically sound.

2.4 X-ray Absorption Near-Edge Structure (XANES) Spectroscopy

The XANES experiments presented in this thesis have been obtained from two different facilities, beamline 20B, the ANBF, Photon Factory and beamline 16A1 at the National Synchrotron Radiation Research Center (NSRRC) Hsinchu, Taiwan. XANES obtained from both beamlines were used to examine the oxidation states of selected cations in the $Ba_2LnSn_xB'_{1-x}O_{6-\delta}$ series (Ln = Pr, Nd or Tb and B' = Nb or Sb). These two beamlines were used because of the different range of energies available from each. Beamline 20B was used where higher energy X-rays were required to examine the Tb L-edge (7.5 keV) and beamline 16A1 was used where lower energy X-rays were required to examine the Sn and Sb L-edges (3.9-4.7 keV). Both beamlines were used to examine the Pr L-edge.

Subsequent to data collection the spectra were normalised using either the BACKSUB procedure in EXAFSPAK[36] or SPLINE in XFIT[37]. Spectra normalised using the two different procedures were not directly compared to each other. Spectra were then plotted in Microsoft Excel or Microcal Origin to allow a comparison of the shape and energy of the absorption edges between different spectra. In the case of the Pr and Tb L-edges principal component, target transformation and multiple linear regression analyses of the XANES spectra were carried out using the PCA, TARGET and DATFIT programs in EXAFSPAK[36, 38], respectively to more thoroughly characterise and quantitatively determine the oxidation state of the lanthanides throughout these series.

2.4.1 XANES at the Australian National Beamline Facility

The optical setup used for XANES measurement at the ANBF is the same as the apparatus required for X-ray diffraction mode up until the sample reaches the Debye-Scherre diffractometer and is described in Section 2.2.2.1. In XANES mode the diffractometer serves merely as a vacuum chamber to reduce the background of the spectra collected. After passing through this the X-rays are incident on an ion counter and then subsequently onto the sample (see Figure 2.12). In the case of these experiments transmission mode was utilised with the absorption of the sample, diluted

in boron nitride, being determined by measuring the intensity of the X-ray beam both before and after the sample using ion chambers. The diluted samples were held between Kapton tape in 1 mm thick sample holders that could accommodate up to 12 samples. The Si (111) monochromator provides highly monochromatic X-rays giving good energy resolution (a E/ΔE of 2400). Spectra were collected of the L_{III}-edge of Tb and Pr with a count time of 1 second per step and a step size of 0.2 eV near the absorption edge. The energy of the XANES spectra of the Pr-L_{III} edge were calibrated using the Cr K-edge of a foil consisting of 10 % Cr in steel. The Tb-L_{III} edge XANES spectra were not calibrated due to problems with the Co foil selected to be used as a reference.

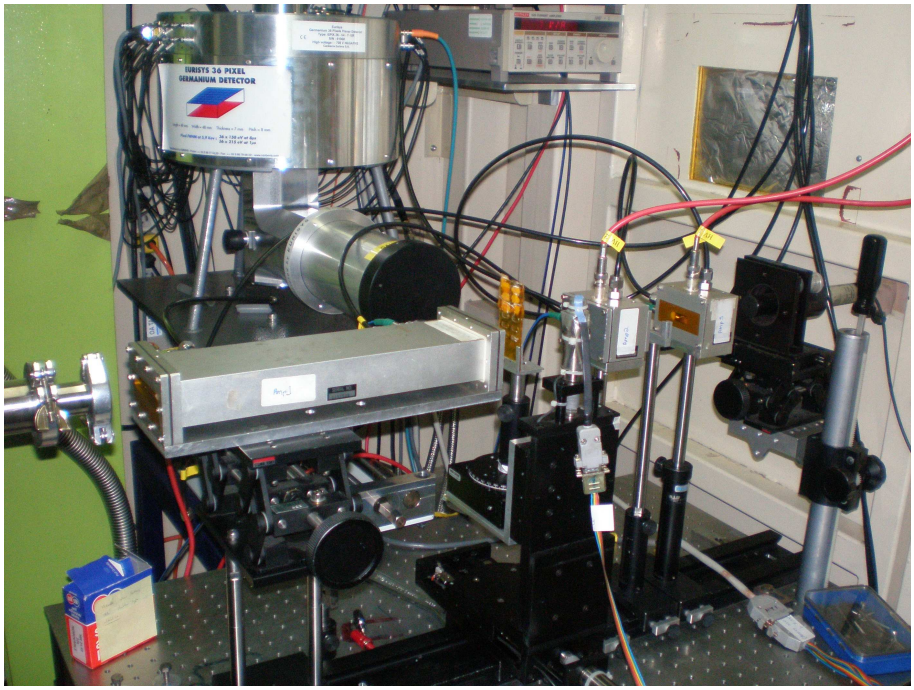

Figure 2.12: Picture of the equipment used to measure the XANES spectra of compounds at the ANBF in transmission mode.

2.4.2 Beamline 16A1 NSRRC

Beamline 16A1 is a medium energy X-ray beamline designed to utilise X-rays over the range of 1-9 kev[39, 40]. Once X-rays leave the ring shielding they pass through a graphite filter and slit aperture before vertical collimation using a water-cooled glidcop mirror. The X-ray beam utilised in the experiments presented in this work was then monochromated using a Si (111) double crystal monochromator before reflecting

off a toroidal focusing mirror and then a high-order-harmonic light rejection mirror before reaching the sample. The samples were examined using fluorescence mode with the fluorescent X-rays being detected using a Lytle detector. Using the Si (111) monochromator on the beamline provided excellent resolution (a E/ΔE of 7000) with an intensity of approximately 3×10^{11} photons/second at the sample[39]. Data were collected over the L-edge regions of Sn, Sb and Pr in steps as small as 0.2 eV near the absorption edges of interest with a count rate of two seconds per step being utilised. The energy of spectra were calibrated using a single collection of the K-edge of a Cr foil.

2.5 Scanning Electron Microscopy (SEM) and Energy Dispersive X-ray (EDX) Analysis

SEM was used to examine the morphology of selected samples and, in combination with EDX analysis, enabled the elemental composition of the phases present to be determined. In this context backscattered electron images were particularly useful as they provide a compositional contrast between light and heavy elements as opposed to the topographic contrast exhibited by secondary electrons[41].

Samples were prepared as sintered pellets produced by applying 10 tons of pressure onto a 13 mm disc. These pellets were then heated overnight at approximately 100 °C less than the maximum temperature used in preparing the sample. The pellets were mounted on standard sample holders using a carbon based paint and then carbon coated to prevent charging effects. The SEM and accompanying EDX analysis was carried out using a Phillips XL 30 SEM, with a tungsten filament operating at 25 keV, a spot size setting of 5 and a working distance of 11 mm. The EDX analysis of elemental composition, was performed in conjunction with the imaging process under the DX-4eDX ZAF operating system (Version 3.3). Analysis was performed using the proprietary software in this system. EDX spectra were produced with scan times averaging 90 seconds. It should be noted that ideally samples examined by EDX should be fixed in resin and polished to make a flat surface, however due to the large number of compounds examined in this study this was not considered to be practical particularly since these results were of secondary interest to this work.

2.6 X-ray Fluorescence (XRF) Spectroscopy

XRF spectroscopy was used to semi-quantitatively or quantitatively determine the bulk chemical composition of selected samples. These measurements were carried out using an Oxford Instruments ED2000 using a standard instrument setting appropriate to the cations being analysised. All measurements were carried out under vacuum with each sample being analysised six times with a counting time of between 2 and 4 minutes per analysis. Where quantitative analysis was required standards containing an appropriate ratio of oxides and carbonates of the cations being analysised were accurately weighted out and thoroughly ground for at least 30 minutes. Regression analysis of these standards was carried out using the proprietary operating system and subsequently this analysis was used to obtain quantitative values of the cations present.

2.7 Thermogravimetric Analysis (TGA)

Selected $Ba_2LnSn_xB'_{1-x}O_{6-\delta}$ (Ln = Pr, Nd or Tb and B' = Nb or Sb) samples were analysised by TGA utilising a SETARAM TAG24 simultaneous differential thermal and thermogravimetric analyser. Data were recorded under two types of atmospheres; 3.5 % H_2 in N_2 and pure N_2 in order to examine weight loss under reducing and inert conditions respectively. Samples were analysised up to a maximum temperature of 960 °C using a heating rate of 5 °/minute.

2.8 Impedance Spectroscopy

Samples of $Ba_2NdSn_xSb_{1-x}O_{6-\delta}$ were selected for analysis via impedance spectroscopy to determine their bulk conductivity. 6 mm diameters pellets of these samples were pressed under a mass of 2 tons and heated at 1300 °C for 60 hrs with the density of the pellets being subsequently determined using the Archimedes method. Gold was then sputter coated onto both faces of the pellets, with care taken not to coat the sides. Pellets were placed into a purpose built sample holder with platinum sheet electrodes spot welded to a gold wire. The gold-coated faces of the sample were held in intimate contact with the platinum sheets of the holder. The wires were connected to a Hewlett Packard 4192ALF Impedance Analyser that was used for the impedance

measurements. Measurements were taken at 50 °C intervals from 400-750 °C, in air, in the frequency range 1-10^6 HZ. Fifteen minutes stabilisation time was allowed at each temperature.

2.9 Ultra-Violet, Visible and Near-Infrared (UV-Vis-NIR) Spectroscopy

UV-Vis-NIR spectra of samples were measured using a Cary 5E UV-Vis-NIR spectrometer equipped with a diffuse reflectance attachment. Scans were usually taken between 200-2500 nm, using a data interval of 0.667 nm and a scanning rate of 200 nm/minute. Polytetrafluoroethylene (PTFE) was used as the background for baseline scans with a standard correction being applied.

2.10 Density Functional Theory (DFT) Calculations

To verify the symmetry and geometry of the crystal structure of Ba_2LaTaO_6 first principles calculations were performed within the framework of Density Functional Theory (DFT). The projector augmented wave method (PAW)[42, 43], as implemented in the Vienna *ab initio* simulation package (VASP)[44, 45], was used with the Perdew-Burke-Ernzerhof (PBE)[46] form of the generalized gradient approximation (GGA). Atomic positions, unit cell volume and shape were optimized using a plane-wave energy cut-off 500 eV and the Brillouin zone sampling with a 4x4x3 k-point Monkhorst-Pack[47] mesh (24 irreducible k-points). The symmetry unconstrained optimization was carried out using a quasi-Newton algorithm until the Hellmann-Feynman forces were less than 0.001 eV/Å on each atom.

2.11 ISOTROPY

ISOTROPY[48] has been used to suggest possible space groups that can be adopted by oxygen deficient double perovskites. It is designed to display information about space groups, their irreducible representations and determine isotropy subgroups. For further explanation regarding the theory behind and use of ISOTROPY consult the manual accompanying the software[48].

2.12 References

[1] D.K. Smith, Gem Dugout Homepage. www.thegemdugout.com (06/06/2008).

[2] R.F. Garrett, D.J. Cookson, G.J. Foran, T.M. Sabine, B.J. Kennedy, S.W. Wilkins, Rev. Sci. Instrum. 66 (1995) 1351-1353.

[3] Z. Barnea, D.C. Creagh, T.J. Davis, R.F. Garrett, S. Janky, A.W. Stevenson, S.W. Wilkins, Rev. Sci. Instrum. 63 (1992) 1069-1072.

[4] R.F. Garrett, The Australian National Beamline Facility. http://old-www.ansto.gov.au/natfac/asrp1.html (21/08/2007).

[5] T.M. Sabine, B.J. Kennedy, R.F. Garrett, G.J. Foran, D.J. Cookson, J. Appl. Crystallogr. 28 (1995) 513-517.

[6] J.R. Hester, PPDA. http://anbf2.kek.jp/ppda/ppdapage.html (06/06/2008).

[7] M. Yamakata, S. Goto, T. Uruga, K. Takeshita, T. Ishikawa, Nucl. Instrum. Methods Phys. Res., Sect. A 467-468 (2001) 667-669.

[8] E. Nishibori, M. Takata, K. Kato, M. Sakata, Y. Kubota, S. Aoyagi, Y. Kuroiwa, M. Yamakata, N. Ikeda, Nucl. Instrum. Methods Phys. Res., Sect. A 467-468 (2001) 1045-1048.

[9] M. Takata, E. Nishibori, K. Kato, Y. Kubota, Y. Kuroiwa, M. Sakata, Adv. X-Ray Anal. 45 (2002) 377-384.

[10] M.M. Elcombe, Bragg Institute: Neutron Scattering at HIFAR; High-Resolution Powder Diffractometer (HRPD). http://www.aaec.gov.au/ansto/bragg/hifar/hrpd.html (22/08/2007).

[11] C.J. Howard, C.J. Ball, R.L. Davis, M.M. Elcombe, Aust. J. Phys. 36 (1983) 507-518.

[12] A.J. Studer, Neutron Scattering at HIFAR: Cryofurnace for HRPD, MRPD and 3-Axis Spectrometer.
http://www.aaec.gov.au/ansto/bragg/ancillaries/cryofurnace.html (11/08/2008).

[13] M. Avdeev, Bragg Institute: Neutron Scattering at HIFAR; Medium-Resolution Powder Diffractometer (MRPD). http://www.aaec.gov.au/ansto/bragg/hifar/med.html (22/08/07).

[14] S.J. Kennedy, Adv. X-Ray Anal. 38 (1995) 35-46.

[15] S. Poulton, High Resolution Powder Diffractometer - BT1.
http://www.ncnr.nist.gov/instruments/bt1/ (06/06/2008).

[16] J.K. Stalick, E. Prince, A. Santoro, I.G. Schroder, J.J. Rush, Mater. Res. Soc. Symp. Proc. 376 (1995) 101-106.

[17] R.I. Smith, ISIS Spallation Neutron & Muon Source: Instruments and Support: Crystallography: Polaris. http://www.isis.rl.ac.uk/crystallography/polaris/ (11/06/08).

[18] R.I. Smith, S. Hull, A.R. Armstrong, Mater. Sci. Forum 166-169 (1993) 251-256.

[19] S. Hull, R.I. Smith, W.I.F. David, A.C. Hannon, J. Mayers, R. Cywinski, Physica B 180-181 (1992) 1000-1002.

[20] R.I. Smith, S. Hull, *User Guide for the Polaris Powder Diffractometer at ISIS*; Rutherford Appleton Laboratory Report: 1997.

[21] R.A. Young, (Ed.), *The Rietveld Method*, Oxford University Press, Chester, 1993.

[22] C.J. Howard, S.J. Kennedy, Mater. Forum 18 (1994) 155-176.

[23] R.B. Von Dreele, in: D.L. Bish, J.E. Post (Ed.), *Modern Powder Diffraction*, Mineralogical Society of America, Washington D.C., 1989, p. 333-369.

[24] R.M. Ibberson, W.I.F. David, K.S. Knight, *The High Resolution Neutron Powder Diffractometer (HRPD) at ISIS - A User Guide*; Rutherford Appleton Laboratory Report: 1992.

[25] D.R. Lide, (Ed.), *CRC Handbook of Chemistry and Physics*, CRC Press, Boca Raton, 2001.

[26] C.J. Howard, B.J. Kennedy, P.M. Woodward, Acta Cryst. B 59 (2003) 463-471.

[27] C.J. Howard, H.T. Stokes, Acta Cryst. B 54 (1998) 782-789.

[28] H.M. Rietveld, J. Appl. Crystallogr. 2 (1969) 65-71.

[29] K.S. Aleksandrov, Ferroelectrics 14 (1976) 801-805.

[30] H. Ibach, H. Lüth, *Solid-State Physics: An Introduction to Principles of Materials Science*, Springer-Verlag, Berlin, 1995.

[31] C.J. Howard, K.S. Knight, B.J. Kennedy, E.H. Kisi, J. Phys.: Condens. Matter 12 (2000) L677-L683.

[32] A.M. Glazer, Acta Cryst. B 28 (1972) 3384-3392.

[33] A.M. Glazer, Acta Cryst. A 31 (1975) 756-762.

[34] B.A. Hunter, C.J. Howard, *A Computer Program for Rietveld Analysis of X-Ray and Neutron Powder Diffraction Patterns*; Lucas Heights Laboratories: 1998.

[35] A.C. Larson, R.B. Von Dreele, *General Strucuture Analysis System (GSAS)*; Los Alamos National Laboratory: 1994.

[36] G.N. George, I.J. Pickering, *EXAFSPAK : A Suite of Computer Programs for Analysis of X-Ray Absorption Spectra*; Stanford Synchrotron Radiation Laboratory: 2000.

[37] P.J. Ellis, H.C. Freeman, J. Synchrotron Radiat. 2 (1995) 190-195.

[38] G.N. George, I.J. Pickering, *Principal Component Analysis and Target Transformation Using EXAFSPAK: Notes for Version 0.1*; Stanford Synchrotron Radiation Laboratory: 2002.

[39] T.-E. Dann, S.-C. Chung, L.-J. Huang, J.-M. Juang, C.-I. Chen, K.-L. Tsang, J. Synchrotron Radiat. 5 (1998) 664-666.

[40] L.-Y. Jang, S.-H. Chang, BL15A DCM Tender X-Ray Beamline. http://140.110.203.42/bldoc/15BDCM1-9.htm (27/09/2007).

[41] I.M. Watt, *The Principles and Practise of Electron Microscopy*, Cambridge University Press, Cambridge, 1997.

[42] G. Kresse, D. Joubert, Phys. Rev. B 59 (1999) 1758-1775.

[43] P.E. Blöchl, Phys. Rev. B 50 (1994) 17953-17979.

[44] G. Kresse, J. Furthmüller, Phys. Rev. B 54 (1996) 11169-11186.

[45] G. Kresse, J. Hafner, Phys. Rev. B 47 (1993) 558-561.

[46] J.P. Perdew, K. Burke, M. Ernzerhof, Phys. Rev. Lett. 77 (1996) 3865-3868.

[47] H.J. Monkhorst, J.D. Pack, Phys. Rev. B 13 (1976) 5188-5192.

[48] H.T. Stokes, D.M. Hatch, B.J. Campbell, ISOTROPY. http://stokes.byu.edu/isotropy.html (21/05/2008).